PROGRESS ON THE HOUGHTON
COLLEGE FUSOR

By

Steven Raymond

A thesis submitted in partial fulfillment of the
requirements for the degree of

Bachelor of Science

Houghton College

June 2020

Signature of Author……………………………………………………………………………..
Department of Physics
June 6, 2020

……………………………………………………………………………………………………....
Dr. Mark Yuly
Professor of Physics
Research Supervisor

……………………………………………………………………………………………………....
Dr. Brandon Hoffman
Professor of Physics

PROGRESS ON THE HOUGHTON COLLEGE FUSOR

By

Steven Raymond

Submitted to the Department of Physics
on June 6, 2020 in partial fulfillment of the
requirement for the degree of
Bachelor of Science

Abstract

Inertial electrostatic confinement (IEC) is an approach to controlled nuclear fusion that uses electrostatic fields to confine the plasma. One type of IEC device, similar to the "fusor" design described in the 1968 patent application [10] by Philo T. Farnsworth, has been constructed at Houghton College. The device consists of two concentric spherical wire mesh electrodes inside a vacuum chamber. A potential of up to -30 kV can be applied to the inner cathode electrode relative to the grounded outer anode electrode. Low pressure gas admitted into the chamber becomes ionized, the positive ions are accelerated towards and fall through the inner negative cathode grid, forming a virtual anode near the center. These ions then oscillate between the outer anode and inner virtual anode. Because of the energies involved, if filled with deuterium gas nuclear fusion reactions would occur. The Houghton College Fusor is currently being modified to prevent sparking at the cathode stalk and configured for remote operation.

Thesis Supervisor: Dr. Mark Yuly
Title: Professor of Physics

CONTENTS

TABLE OF FIGURES

Chapter 1

INTRODUCTION

1.1.   *History of Controlled Nuclear Fusion*

Nuclear fusion occurs when two nuclei are close enough that the strong nuclear force can bind the two nuclei together into one larger nucleus. This process releases energy for light nuclei, and is the mechanism which powers stars. Because a nuclear fusion reaction releases on the order of a million times more energy than a chemical reaction, scientists have attempted to harness controlled nuclear fusion as a source of energy. An example of this can be seen in Figure 1.
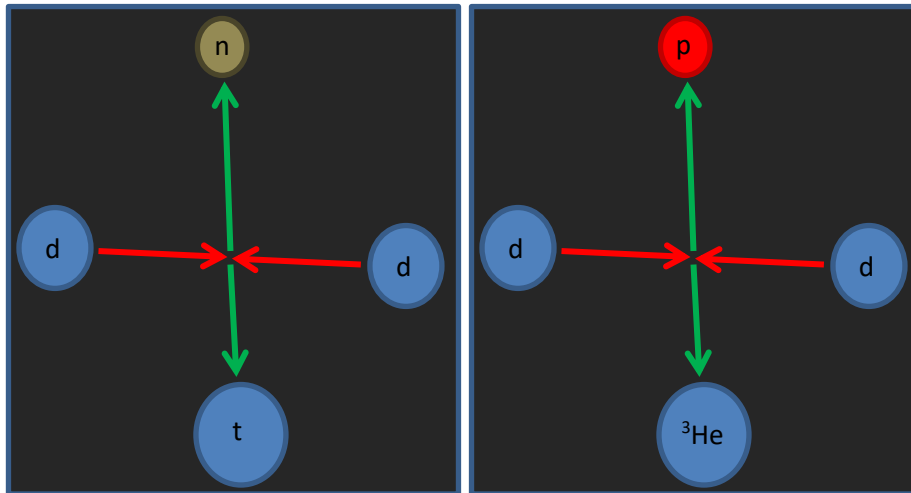
Figure 1. D-D reaction. (Left) d-d reaction producing a neutron and a triton.
(Right) d-d reaction producing a proton and a ^{3}He nucleus.

Nuclear Fusion requires energies on the order of kV or more because the Coulomb repulsion force causes protons to repel. The nuclear strong force is approximately 137 times stronger than the Coulomb repulsion force, but it is a short range force, and the Coulomb force dominates until the nuclei are within about a femtometer. Because of

quantum mechanics, it is possible for a nucleus to fuse if it is farther from the other nucleus than 1 fm, but the probability of this happening decreases exponentially with distance; thus, in order to fuse, two nuclei must be close to each other.

Fusion can be achieved using a particle accelerator, which imparts individual particles with mega-electron volts, or MeVs of energy; however, for producing energy, this is impractical, and in order to maintain a fusion chain reaction, a large number of particles must be confined and brought to fusion temperatures (keVs of energy) in a thermonuclear process. Fusion can release large amounts of energy, for example, the reactions in Figure 1 release 4.03 MeV or 3.27 MeV per reaction, but because of the high temperature, to achieve ignition, where the reactions become self-sustaining, a significant amount of input energy is required. For this reason, isotopes of hydrogen are ideal because of their low Z.

1.2.   Types of fusion

There are three main ways of containing a plasma, which is an ionized gas where the positive ions and the electrons move about freely, and heating it to fusion conditions. The two most successful to date are magnetic confinement fusion (MCF) and inertial confinement fusion (ICF). The method of interest for the research described in this thesis, inertial electrostatic confinement (IEC) fusion has also been used to contain a plasma at fusion conditions. Each method will be discussed in this section

1.2.1. Magnetic Confinement

The two most successful magnetic fusion devices are the tokamak and the stellarator. Tokamaks were invented by Soviet scientists Igor Tamm and Andrei Sakharov in 1950 [1].

In essence they are comprised of a toroidal "solenoid" coil. The coil creates a strong toroidal magnetic field that causes the plasma to circulate throughout the toroid as shown in Figure 2. Because the plasma consists of moving charges, there is a poloidal field created by the plasma that causes it to both be compressed and to rotate. The plasma can be heated in several ways, generally by inducing an electric current through the plasma or by increasing the strength of the toroidal field. The current through the plasma can be increased by increasing the current through the poloidal coils, thereby increasing the toroidal electric field. Because the resistance of the plasma decreases as the temperature of the plasma increases, this method has a limit to how much it can heat the plasma. Heating the plasma can also be done by rapidly increasing the compressing field strength, which is also helpful because in addition to increasing the temperature of the plasma, it also compresses the plasma allowing for more collisions.
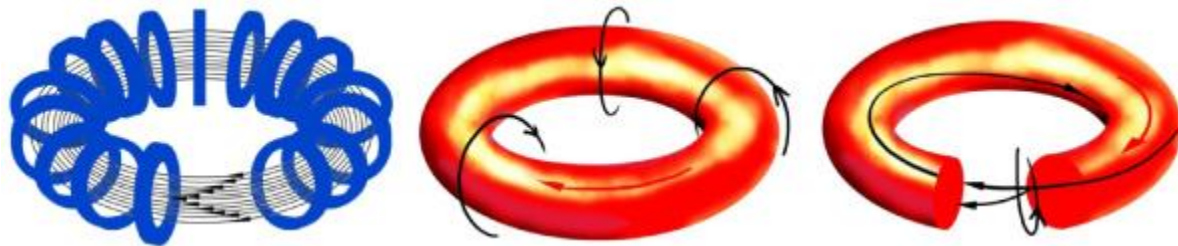
Figure 2. A diagram of a tokamak magnetic field. (Left) A solenoid is wrapped into a toroid and generates a toroidal magnetic field. (Middle) The plasma follows the toroidal magnetic field lines and generates a poloidal field. (Right) The toroidal field and the poloidal field combine to cause the plasma to drift away from the center and towards the edge of the tokamak. Figure taken from Ref. [2].

Currently, research with Tokamaks is being done at research facilities such as the Joint European Torus (JET) [3] and the International Thermonuclear Experimental Reactor (ITER) [4]. Although research is being done with tokamaks, there are still many obstacles. The superconducters used to create the magnetic fields in a tokamak can be damaged by

radiation, which causes the magnets to be less effective. Another problem lies in the inward facing materials in the tokamak, which are also subjected to radiation, which can damage the inward facing materials over time. Additionally, the confinement time of the plasma is dependent on the major and minor axis of the tokamak, and for longer confinement times, a larger tokamak is required.

Stellarators work in a similar manner to tokamaks in the sense that they use strong magnetic fields to confine a plasma. Stellarators were the American attempt at magnetic confinement originally designed by Lyman Spitzer in 1951 [5]. The problem with tokamaks is that because of how the solenoids are bent into a toroidal shape, the magnetic field is stronger near the center of the toroid than at the edges. This causes charged particles to drift away from the magnetic field lines and towards the edges of the chamber. One method of reducing this drift was to use a transformer to introduce a new magnetic field that would twist the plasma and reduce drift. Another method of reducing drift though was to use a stellarator. The initial design that Spitzer proposed was to twist the solenoid into a figure eight shape [5] similar to a Mobius strip as opposed to the toroidal shape of a tokamak. The figure eight shape would cancel out the drift partially. Eventually, Spitzer realized that by wrapping wires helically around the stellarator with alternating current running through the wire, the plasma could be twisted without twisting the solenoid into a figure eight shape. This did not completely eliminate the plasma drift, but with the use of computers, it became possible to shape the magnetic field to further reduce plasma drift as was done with the new Wendlelstein 7-X in Germany [6].

1.2.2. Inertial Confinement

Inertial confinement fusion (ICF) uses a different mechanism to fuse nuclei that is being explored by scientists at the National Ignition Facility (NIF) and the Laboratory for Laser Energetics (LLE). There are two methods of ICF: indirect and direct drive. Direct drive works by placing a small target capsule (generally around 1 mm in diameter) filled with deuterium and tritium, at the center of a chamber and focusing high energy lasers onto the surface of the capsule to compress it isotropically. At LLE, researchers use sixty lasers which are capable of delivering a total energy on target of 40 kJ per pulse [7]to compress the target capsule. The capsule outer surface heats up because of the lasers and ablates, the reaction force from which compresses the fuel inside the capsule, bringing the fuel to fusion conditions within a fraction of a nanosecond. Indirect drive, such as is used at NIF [8], operates in a similar manner, but the high energy lasers are focused on a hohlraum with the target capsule inside of it, which is a small metal cylinder. The hohlraum heats up and emits x-rays which are then focused on the target capsule. Indirect drive is useful because the target capsule can more efficiently absorb the target x-rays, but the hohlraum takes more energy to heat as well. Researchers at NIF use one hundred and ninety-two lasers capable of delivering up to 2.15 MJ [9] of energy on target per shot.

1.2.3. Inertial Electrostatic Confinement

Another technique for controlled nuclear fusion is called inertial electrostatic confinement fusion (IEC). An Inertial electrostatic confinement fusor consists of a vacuum chamber that contains two or more nested gridded electrodes. IEC fusion works by evacuating the chamber to approximately 1×10^{-6} Torr and then allowing gas into the chamber, raising the pressure to approximately 1×10^{-4} Torr. A potential difference is placed across the

electrodes and is increased until the gas becomes ionized. The gas pressure is then lowered and the potential is raised to 10-30 kV. The large (10kV or more) potential difference creates a potential well; the way that the potential well forms depends on how the potential is applied across the electrodes. If the inner electrode is held at a high positive voltage relative to the grounded outer electrode, it becomes an anode. Electrons are then attracted to the center of the anode because it is the lowest point of potential. A plot of electric potential inside an IEC chamber can be seen in Figure 3. The electrons then pass through the anode and travel to the chamber wall, where they are recirculated and repeat the same process. The region where the electron density is highest is the center and the high density of electrons at the center of the anode forms what is called a virtual cathode, which creates a potential well for positive ions. Similarly, if the inner electrode is held at a high negative potential relative to the outer cathode grid, then the cathode grid attracts positive ions to the center, and the ions will begin to form a virtual anode.

1.3.   Development of Inertial Electrostatic Confinement Fusion

Philo Farnsworth was an American scientist who patented the first design for Inertial Electrostatic Confinement in 1966 [10]. Because of Earnshaw's theorem [11], which states that for a given collection of point charges, the charges cannot be held in stable equilibrium via the electrostatic interactions of the point charges, many scientists dismissed the idea that IEC could be used for controlled nuclear fusion. What Farnsworth and other scientists pursuing IEC realized was that Earnshaw's theorem assumed a static system, however, if the ions were able to move while still being confined, they might be capable of confining

the electrons. Farnsworth also realized that for a spherical anode and cathode, confining the ions near the center would result in higher density measured at the center [10].

As shown in Figure 3, Farnsworth designed an IEC Fusor to utilize potential wells that would form within the chamber as a result of the electrodes and the charged plasma. In Farnsworth's original design, the outer electrode was the wall of a vacuum chamber, which was grounded, while the inner electrode was a gridded sphere that was placed at a high positive potential and acted as an anode. Electrons were emitted from the cathode and accelerated towards the center of the chamber because of the massive potential difference; most electrons passed through the center of the anode without collisions, and recirculated. Electrons followed the orbit shown in Figure 4, but due to the large number of electrons, the area of highest electron density was in the center of the anode. The electric potential inside the chamber is shown in Figure 3 and a typical electron orbit is shown in Figure 4. The higher electron density at the center will form a virtual cathode, creating a potential well where positive ions, which were introduced into the chamber via an ion gun, may be trapped.

Depending on the grid openings and the pressure, IEC fusors can be operated in different modes, which is shown in Figure 5: star mode, central spot mode, and halo mode. Each mode is stable and has been reproduced by several experiments, and each mode is associated with a different potential well shape and fusion reaction rate or neutron production rate (NPR), where the NPR is proportional to the cross-section of the neutron producing reaction. The NPR depends on the shape of the potential well because the more

effectively a plasma is contained at a given temperature, the more the fusion reactions per unit volume.
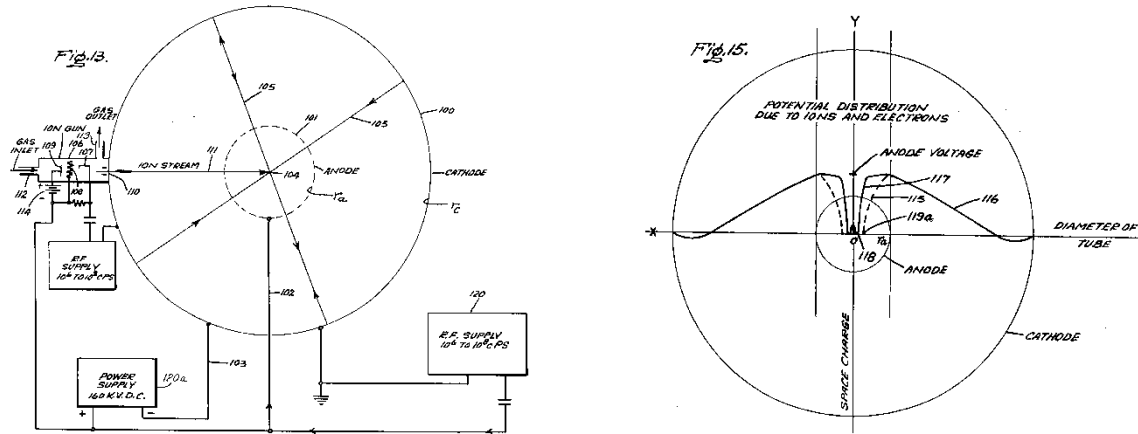
Figure 3. The Farnsworth fusor. (Left) In the original design, the outer chamber was grounded, and the anode was placed at a high positive potential. Electrons were accelerated towards the center of the chamber, and were trapped, forming a virtual cathode. This caused ions born from the ion gun attached to the chamber to accelerate towards the center of the chamber. (Right) Potential as a function of radius. The potential was zero at the grounded chamber walls, but increased for positive ions as they approached the anode. The potential approached zero rapidly once inside the anode due to the virtual cathode. Figure from Ref. 7.
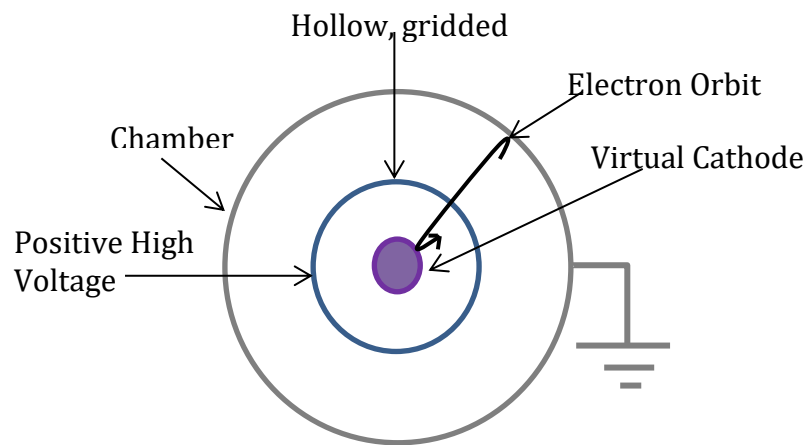
Figure 4. The typical electron orbit. The electron starts near the edges of the chamber, then falls in towards the anode, accelerating across the several kilovolt potential difference. Most Electrons will pass through the anode without collisions and then recirculate, falling back towards the anode. The region of highest electron density is the center of the anode and is what is referred to as a virtual cathode

Central spot mode is characterized by the plasma being confined to a sphere in the center

of the cathode and can be obtained by using a grid with small openings, and thus low grid

transparency. The Halo mode is similar, however there is an electron "jet" from the center

of the cathode grid. IEC devices operate in this mode when the cathode grid has one

opening that is slightly larger than the other openings. In star mode, the plasma is confined

in the center of the cathode grid, however, because of the higher grid transparency,

microchannels or "spokes" radiate out from the center of the cathode grid. The spokes are

ion beams aligned such that they pass through the center of the grid openings. Star mode

has a high neutron production efficiency because the grid openings are larger, allowing

more ions to pass through the core before being intercepted by the grid. Star mode can be

achieved by using larger grid openings than in central spot mode, and thus a higher grid

transparency (95%>) and by operating at lower pressures (< 10 mTorr) and higher

potentials (30>kV).

Figure 5. Operating modes of an IEC device. In central spot mode (left) the plasma is contained in one spot in the center; Figure taken from Ref. [12]. In star mode (center) the plasma is contained in the center of the cathode, but the grid is transparent enough to allow jets of ions to radiate out from the center. Figure taken from Ref. [12]. In halo mode (right) there is one ion jet that radiates out through a point in the grid where the transparency is higher. Figure taken from Ref. [13].

1.4.   History of IEC Devices

After Farnsworth's prototype for an IEC device, more designs were developed to study and understand the behavior of plasmas and the development of potential wells within an IEC fusor in order to improve the performance of the device.

1.4.1. Farnsworth IEC devices

P.T. Farnsworth originally patented his design for an IEC device in 1966 [10]. In his design, a potential was placed across the electrodes with a power supply capable of supplying a 160 kV potential difference. Ions were introduced into the chamber via an ion gun and the ionization fraction was controlled by a RF power supply capable of 10^8 cycles per second.

In 1968, Farnsworth patented another design for an IEC device, shown in Figure 6. His new design operated in a similar manner, but the anode and cathode were switched, and a high negative voltage was applied to the inner electrode. This change affected the internal potential distribution. Because the anode and cathode were switched, ions born near the edge of the chamber were accelerated towards the center of the cathode, and like the electrons in the original design, the ions would pass through the cathode and recirculate, and the region with the highest ion density would be within the cathode. This would cause the creation of a virtual anode, and the ions would oscillate between the real and virtual anode. The virtual anode would create a potential well for electrons and electrons would be accelerated towards the virtual anode, creating a virtual cathode. This process would continue forming multiple nested virtual anodes and cathodes.
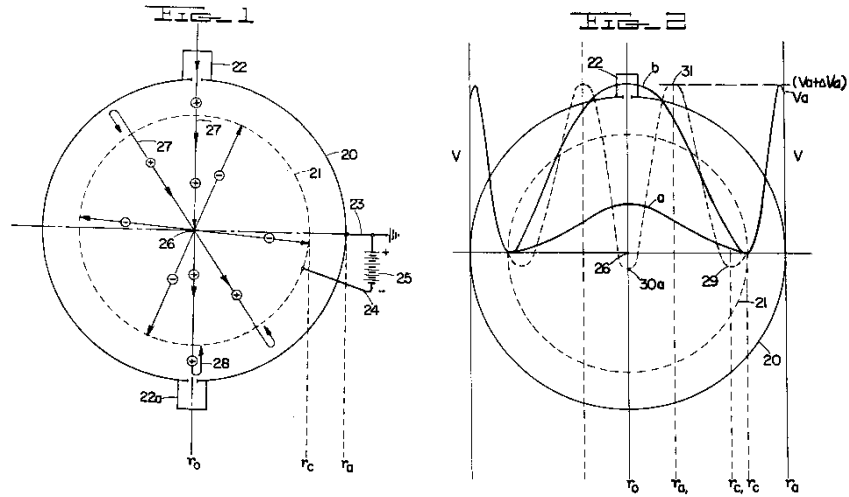
Figure 6. The new design for the Farnsworth fusor. (Left) The anode and the cathode are switched, where r_c is the radius of the cathode and r_a is the radius of the anode. (Right) The potential as a function of radius for Farnsworth's second design. Figures from Ref. [14].

1.4.2. Hirsch's design for an IEC Device

Robert Hirsch worked with PT Farnsworth and Gene Meeks, and in 1970, Hirsch and Meeks patented a new design for the IEC fusor [15]. The device in Figure 7 operated in a similar manner to Farnsworth's design, however, instead of an ion gun, an ion grid source was placed between the outer anode and the cathode. Positive ions formed at this grid were accelerated towards the cathode forming a virtual anode, however, because of the ion grid source, the ion distribution was more symmetric around the cathode. The ion grid source ionized gas because it was held at a positive high voltage and attracted electrons produced by a thermionic cathode. The electrons were attracted to the grid and would oscillate around it, ionizing gas introduced to the chamber near the grid. Additionally, the cathode and ion source were made to have larger openings in the grid, allowing more electrons and ions to avoid collisions with the spherical mesh.

15
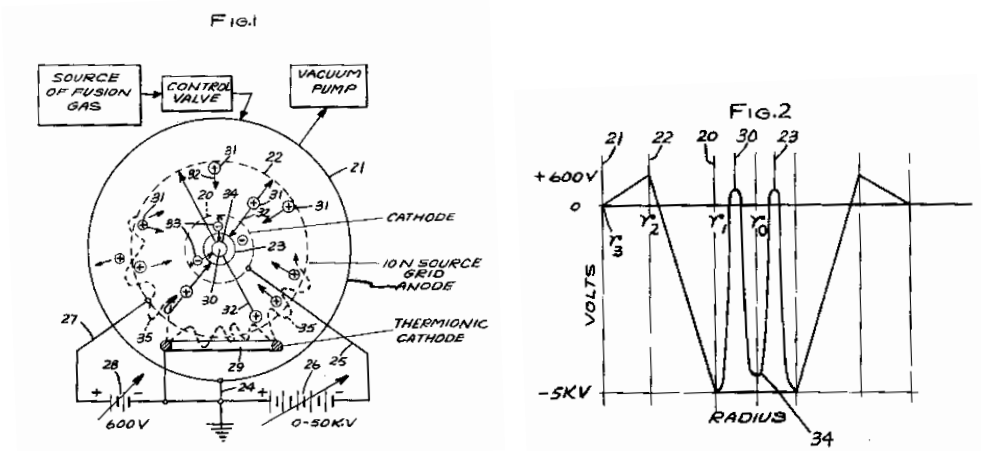
Figure 7. The Farnsworth-Hirsch fusor design. (Left) The design for the Farnsworth-Hirsch Fusor. The thermionic cathode produced electrons, which were attracted to the ion source grid. Electrons near the grid ionized gas near the grid, and the ions were accelerated towards the cathode. Figure from Ref. [15]. (Right) Potential as a function of radius inside the Farnsworth-Hirsch fusor. In the diagram R_0 marks the center of the chamber and the virtual cathode, R_1 marks the cathode, the two peaks between R_0 and R_1 mark the virtual anode, R_2 marks the ion source grid, and R_3 marks the anode. Figure from Ref. [15].

1.5.   IEC at Houghton

Houghton College is currently working on a Farnsworth fusor, for the purposes of studying nuclear reactions and the behavior of plasmas. As an example, the ^{2}H(d,n) ^{3}He reaction could be studied, or it could be used to produce neutrons for neutron scattering and activation experiments. Additionally, the properties of the plasma as a function of the geometry of the electrodes could be studied using Langmuir probes, atomic spectroscopy, or neutron production.

The IEC device at Houghton can also be used as an x-ray source. By using the fusor as an x-ray source, researchers at Houghton could study the biological effects of x-rays and the

effects of x-rays on a polymer's physical and chemical properties. The fusor could also be used for studying materials via x-ray fluorescence and x-ray diffraction.

Chapter 2

THEORY

The design of an IEC fusor is relatively straightforward, but the theory behind how it works

is complex. For an IEC fusor to work, it must create and confine a stable plasma, which

requires ions to be trapped within a cathode grid. In order to understand how an IEC fusor

works then, it is important to better understand both the behavior of the plasma and how

potential wells form and how they are able to maintain a stable plasma. Thus, the formation

of potential wells will be discussed in this chapter as well as governing equations for a

plasma.

2.1.   Potential Wells

Potential wells have already been briefly touched on, but in order to understand how an

IEC device works, it is important to discuss in more detail how potential wells form. In a

Farnsworth-Hirsch Fusor (shown in Figure 7 and Figure 8), a spherical gridded anode is

placed inside a spherical metal vacuum chamber, which is grounded. Nested within the

anode is a spherical gridded cathode which is held at a negative potential, generally tens of

kilovolts or more relative to the anode. The cathode forms a potential well for positive ions.

Because of the low potential at the center of the cathode, positive ions within the chamber

are accelerated towards the center of the chamber. Unless the positive ions have enough

energy to break free of the negative potential well, the ions will be trapped within the

cathode grid. Ions with enough energy to escape the potential well either collide with other

particles within the potential well, or pass through the center of cathode grid towards the

anode, where they are recirculated back into the potential well. The ions trapped inside the

potential well begin to build up inside the cathode forming what is called a virtual anode. Because of the buildup of positive charge within the cathode, electrons are then attracted to the virtual anode and begin to build up inside of the virtual anode, forming a virtual cathode and a second potential well. This process can continue, and multiple nested virtual anodes and cathode can form, creating multiple potential wells within the cathode.
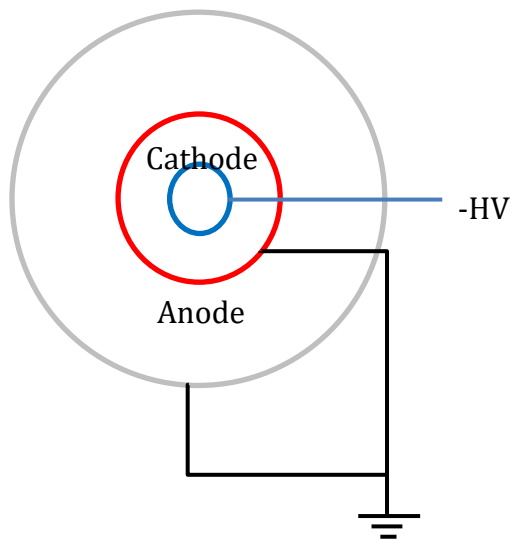

Figure 8. A diagram of a Farnsworth-Hirsch Fusor. The outer chamber (grey), and the anode (red) are grounded, while the cathode (blue) is held at a negative high voltage.
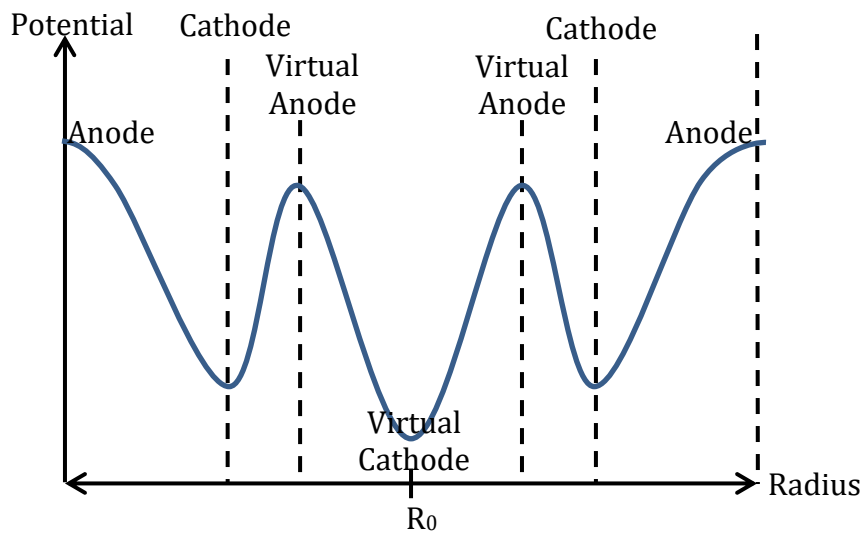
2.2. *Plasma Equations*

In order to understand what happens inside an IEC fusor, it is important to understand the behavior of the plasma inside of the fusor, which is described by an equation of motion for the plasma. The derivation below follows the derivation from Callen [16]. For a plasma consisting of a single particle, we can describe the position of a particle in a 6-D phase space with coordinates of position and velocity,

$$N(\boldsymbol{x}, \boldsymbol{v}, t) = \delta(\boldsymbol{x} - \boldsymbol{X}(t))\delta(\boldsymbol{v} - \boldsymbol{V}(t)) \tag{2.1}$$

where N($\mathbf{x}$, $\mathbf{v}$, t) is the density distribution function of the point particle, and $\mathbf{X}$(t) and $\mathbf{V}$(t) describe the position and velocity, respectively, of the particle (x, y, z, v_x, v_y, v_z) in phase space at time t. The density distribution function can be used to describe the probability of a given particle density.

The distribution function in 3-D position phase space for a single particle with a trajectory of $\mathbf{X}$(t) can be described by the delta function $\delta(\boldsymbol{x} - \boldsymbol{X}(t)) = \delta(x - X(t))\delta(y - Y(t))\delta(z - Z(t))$, where $\mathbf{X}$(t), $\mathbf{Y}$(t), and $\mathbf{Z}$(t) describe the position of the partical in 3-D phase space, and the distribution function for a single particle in 3-D velocity space velocity space can be described in a similar manner $\delta(\boldsymbol{v} - \boldsymbol{V}(t))$. Here, $\mathbf{x}$, $\mathbf{v}$ are Eulerian coordinates in 6-D phase space and are fixed coordinates, and $\mathbf{X}$(t), $\mathbf{V}$(t) are Lagrangian coordinates moving with the particle.

Each individual particle in the gas can be described by a coordinate in phase space in this manner. Therefore, for a given region of phase space, the microscopic distribution function is:

$$N_s^m(\boldsymbol{x}, \boldsymbol{v}, t) = \sum_{i=1}^{N_0} \delta(\boldsymbol{x} - \boldsymbol{X}_i(t))\delta(\boldsymbol{v} - \boldsymbol{V}_i(t)). \qquad (2.2)$$

The subscript s refers to the species of particle, the m denotes that this is a microscopic system, and N_0 is the total number of species s. To understand the meaning of N, consider $dN = N(\boldsymbol{x}, \boldsymbol{v}, t)d^3x d^3v$, the number of particles in a differential volume of 6-D phase space given by $\boldsymbol{x}$ = d$\boldsymbol{x}$, $\boldsymbol{v}$ + d$\boldsymbol{v}$. N, therefore, can be considered as the number density at a particular point in 6-D phase space. The distribution function in Equation (2.2) can be normalized such that integrating over all velocity space gives the particle number density with units of (number/volume):

$$dN(\boldsymbol{x}, t) = \frac{dN}{d^3x} = \int d^3v \, N^m(\boldsymbol{x}, \boldsymbol{v}, t) = \sum_{i=1}^{N_0} \delta(\boldsymbol{x} - \boldsymbol{X}_i(t)). \qquad (2.3)$$

Integrating the particle density over a volume V gives the total number of particles N in the volume V

$$\int_V d^3x \, dN(\boldsymbol{x}, t) = N, \qquad (2.4)$$

therefore, the total number of particles N in a volume V of 6-D phase space is given by

$$N = \int_{All\ Velocities} \int_V dN(\boldsymbol{x}, t) d^3x\, d^3v$$

(2.5)

By taking the time derivative of the density distribution function, the equation of motion for the plasma can be obtained

$$\frac{dN_s(\boldsymbol{x}, \boldsymbol{v}, t)}{dt} = \left[\frac{\partial}{\partial t} + \frac{\partial \boldsymbol{x}}{\partial t} \cdot \boldsymbol{\nabla}_x + \frac{\partial \boldsymbol{v}}{\partial t} \cdot \boldsymbol{\nabla}_v \right] \sum_{i=1}^{N_0} \delta(\boldsymbol{x} - \boldsymbol{X}_i(t)) \delta(\boldsymbol{v} - \boldsymbol{V}_i(t)).$$

(2.6)

Rewriting the partial time derivative gives

$$\frac{dN_s(\boldsymbol{x}, \boldsymbol{v}, t)}{dt} = \left[\left(-\frac{\partial \boldsymbol{X}_j}{\partial t} \cdot \boldsymbol{\nabla}_x - \frac{\partial \boldsymbol{V}_j}{\partial t} \cdot \boldsymbol{\nabla}_v \right) + \left(\frac{\partial \boldsymbol{x}_j}{\partial t} \cdot \boldsymbol{\nabla}_x + \frac{\partial \boldsymbol{v}_j}{\partial t} \cdot \boldsymbol{\nabla}_v \right) \right]$$

$$\left(\sum_{i=1}^{N_0} \delta(\boldsymbol{x} - \boldsymbol{X}_j(t)) \delta(\boldsymbol{v} - \boldsymbol{V}_j(t)) \right) = 0.$$

(2.7)

We can set the time derivative of N_s equal to zero because the only time when the delta functions are non-zero is when $\boldsymbol{x} = \boldsymbol{X_i}$ and $\boldsymbol{v} = \boldsymbol{V_i}$, and when this is the case, the derivatives cancel. Showing that $dN_s/dt = 0$ is done using the properties of delta functions that $(\partial/\partial t)\delta(\boldsymbol{x} - \boldsymbol{X}(t)) = (-d\boldsymbol{x}/dt) \cdot (\boldsymbol{\nabla}_x)\delta(\boldsymbol{x} - \boldsymbol{X}(t))$ and $\boldsymbol{x}\delta(\boldsymbol{x} - \boldsymbol{X}(t)) = \boldsymbol{X}(\boldsymbol{x} - \boldsymbol{X}(t))$, as well as similar properties for velocity. Therefore, Equation (2.6) can be rewritten as

$$\frac{dN_s(\boldsymbol{x},\boldsymbol{v},t)}{dt} = \sum_{i=1}^{N_0} \left[\frac{\partial}{\partial t} + \frac{\partial \boldsymbol{x}}{\partial t} \cdot \boldsymbol{\nabla}_x + \frac{\partial \boldsymbol{v}}{\partial t} \cdot \boldsymbol{\nabla}_v \right] \delta\big(\boldsymbol{x} - \boldsymbol{X}_i(t)\big)\delta\big(\boldsymbol{v} - \boldsymbol{V}_i(t)\big) = 0. \tag{2.8}$$

Using Equation (2.2), Equation (2.8) can be rewritten as

$$\frac{\partial N_s}{\partial t} = -\frac{\partial \boldsymbol{x}}{\partial t} \cdot \boldsymbol{\nabla}_x N_s - \frac{\partial \boldsymbol{v}}{\partial t} \cdot \boldsymbol{\nabla}_v N_s. \tag{2.9}$$

Taking these derivatives, the equation of motion is given by

$$\frac{\partial N_s(\boldsymbol{x},\boldsymbol{v},t)}{\partial t} = -\boldsymbol{v} \cdot \boldsymbol{\nabla}_x N_s - \boldsymbol{a} \cdot \boldsymbol{\nabla}_v N_s. \tag{2.10}$$

Using the Newton-Lorenz force, acceleration can be rewritten

$$\boldsymbol{a} = \frac{1}{m}[q\boldsymbol{E}(\boldsymbol{X}_i(t),t) + q\boldsymbol{V}_i(t) \times \boldsymbol{B}(\boldsymbol{X}_i(t),t)], \tag{2.11}$$

where the electric and magnetic field can be determined using the Maxwell equations

$$\boldsymbol{\nabla} \cdot \boldsymbol{E} = \frac{\rho}{\epsilon_0}, \tag{2.12}$$

$$\boldsymbol{\nabla} \times \boldsymbol{E} = -\frac{\partial \boldsymbol{B}}{\partial t}, \tag{2.13}$$

$$\boldsymbol{\nabla} \cdot \boldsymbol{B} = 0, \tag{2.14}$$

and:

$$\nabla \times \boldsymbol{B} = \frac{1}{c^2} \frac{\partial \boldsymbol{E}}{\partial t} + \mu_0 \boldsymbol{J}, \tag{2.15}$$

where the microscopic charge $\rho(\boldsymbol{x}, t)$ and current $\boldsymbol{J}(\boldsymbol{x}, t)$ source densities are obtained by integrating the distribution function over velocity space as was done in Equation (2.2). Summing over species s yields

$$\rho(\boldsymbol{x}, t) \equiv \sum_s q_s \int_{All\ velocities} N_s(\boldsymbol{x}, \boldsymbol{v}, t) d^3 v = \sum_s q_s \sum_{i=1}^{N_0} \delta(\boldsymbol{x} - \boldsymbol{X}(t)) \tag{2.16}$$

and:

$$\boldsymbol{J}(\boldsymbol{x}, t) \equiv \sum_s q_s \int_{All\ velocities} \boldsymbol{v} N_s(\boldsymbol{x}, \boldsymbol{v}, t) d^3 v = \sum_s q_s \sum_{i=1}^{N_0} \boldsymbol{v}_i \delta(\boldsymbol{x} - \boldsymbol{X}(t)), \tag{2.17}$$

where q_s is the charge of the ion species. Using Equation (2.11) to rewrite acceleration, the equation of motion for the plasma can be rewritten as

$$\frac{\partial N_s(\boldsymbol{x}, \boldsymbol{v}, t)}{\partial t} = -\boldsymbol{v} \cdot \nabla_x N_s - \frac{q_s}{m_s} [\boldsymbol{E}^m(\boldsymbol{X}_i(t), t) + q\boldsymbol{V}_i(t) \times \boldsymbol{B}^m(\boldsymbol{X}_i(t), t)] \cdot \nabla_v N_s \tag{2.18}$$

where m stands for microscopic because the electric and magnetic fields are due to the individual particles within the plasma. Finally, using the property of the dirac delta that:

$$a\delta(a-b) = b\delta(a-b) \qquad (2.19)$$

we can rewrite all the $\mathbf{X_i}$ as $\mathbf{x}$ and all the $\mathbf{V_i}$ with $\mathbf{v}$, and rewrite Equation (2.18) as

$$\frac{\partial N_s(\boldsymbol{x},\boldsymbol{v},t)}{\partial t} = -\boldsymbol{v}\cdot\boldsymbol{\nabla}_x N_s - \frac{q_s}{m_s}[\boldsymbol{E^m}(\boldsymbol{x},t) + q\boldsymbol{v}\times\boldsymbol{B^m}(\boldsymbol{x},t)]\cdot\boldsymbol{\nabla}_v N_s. \qquad (2.20)$$

This is the Klimontovich equation. Equations (2.12) through (2.20) and the initial conditions of the particles describe the motion of the particles in the plasma. The Klimontovich equation is exact, however, it is practically impossible to solve because of the amount of information required for individual particles. Because of this, it is helpful to find the average of the Klimontovich equation as described by Callen [17]. Consider all of the particles within a six-dimensional box in phase space, N6D, where the volume of the box in spatial coordinates is given by $\Delta V_x = \Delta x \Delta y \Delta z$ and the volume velocity-space coordinates is given by $\Delta V_v = \Delta v_x \Delta v_y \Delta v_z$. The number of particles, N6D, is given by

$$N_{6D} \equiv \int_{\Delta V_x} d^3 x \int_{\Delta V_v} d^3 v\, N_s, \qquad (2.21)$$

and the average distribution function $\langle N_s \rangle$ is defined as the number of particles within the box in 6-D phase space, N6D, divided by the volume of the box. The box in phase space must be large enough to neglect the fluctuations in the number of particles in the box, but the box should be small enough that the macroscopic properties of the plasma do not vary widely within the box. In order to satisfy these conditions, the size of the box in physical space must be on the scale of $n^{-\frac{1}{3}} < \Delta x < \lambda_D$ [17], where Δx is the length of the box, $n^{\frac{-1}{3}}$ and λ_D is the Debye length. In velocity space, the size of the box should be $(\frac{v_T}{n\lambda_D^3})^{\frac{1}{3}} < \Delta v_x$ [17], where $v_T \equiv \sqrt{\frac{2T}{m}}$ is the thermal velocity and T is the temperature in Joules or eV [18]. V$_T$ is the most probable speed of the Maxwellian distribution. The Klimontovich equation, averaged over position and velocity, is

$$\frac{d\langle N_s \rangle}{dt} = \left\{ \frac{\partial \langle N_s \rangle}{\partial t} + \boldsymbol{v} \cdot \boldsymbol{\nabla}_x \langle N_s \rangle + \frac{q_s}{m_s} [\boldsymbol{E}(\boldsymbol{x},t) + q\boldsymbol{v} \times \boldsymbol{B}(\boldsymbol{x},t)] \cdot \boldsymbol{\nabla}_v \langle N_s \rangle \right\} = C(f) \qquad (2.22)$$

where $C(f)$ is the Coulomb collision operator [19] on the average distribution function f_s, and accounts for the Coulomb collisions in the plasma. However, if the collisions in the plasma are minimal, then $C(f)$ is zero, giving

$$\frac{d\langle N_s \rangle}{dt} = \left\{ \frac{\partial \langle N_s \rangle}{\partial t} + \boldsymbol{v} \cdot \boldsymbol{\nabla}_x \langle N_s \rangle + \frac{q_s}{m_s} [\boldsymbol{E}(\boldsymbol{x},t) + q_s\boldsymbol{v} \times \boldsymbol{B}(\boldsymbol{x},t)] \cdot \boldsymbol{\nabla}_v \langle N_s \rangle \right\} = 0. \qquad (2.23)$$

This equation is the Vlasov equation. The Vlasov equation is a differential equation whose solutions produce the potentials described in Section 2.1. The average distribution function $\langle N_s \rangle$ can be used to determine the charge and current distribution:

$$\rho(\boldsymbol{x}, t) \equiv \sum_s q_s \langle N_s \rangle d^3 v \tag{2.24}$$

$$\boldsymbol{J}(\boldsymbol{x}, t) \equiv \sum_s q_s \boldsymbol{v} \langle N_s \rangle d^3 v. \tag{2.25}$$

From these equations and Maxwell's equations, **E** and **B** can be determined, however, this method does not "close the loop" because distribution function $\langle N_s \rangle$ depends on **E** and **B**.

Chapter 3

CHAMBER SETUP

In this chapter, the Houghton College Farnsworth fusor is discussed in detail. The physical setup of the fusor as well as the computer code for remotely controlling the fusor is presented, along with the parameters for controlling each component via the computer are discussed in detail.

3.1. The IEC Chamber Setup

The IEC device at Houghton is slightly different than the standard Farnsworth Fusor. Instead of having an anode nested inside the cathode and a grounded chamber, the fusor has a grounded chamber and grounded outer grid and an inner grid that is held at a negative high voltage. The design is similar to the second design for an IEC device that Farnsworth proposed, as seen in Figure 6. The Houghton College fusor is set up such that positive ions are attracted towards the cathode, which is held at negative high voltage. This allows a positive virtual anode to form directly.

The vacuum chamber itself is constructed out of stainless steel and is 0.35 meters in diameter. The chamber has 18 ports of different sizes; these ports are used as viewports, feedthroughs for attaching sensors, or for allowing x-rays to exit the chamber via a thin Mylar window. Attached to the chamber are a Granville-Phillips Convection pirani gauge used for measuring pressures down to 1×10^{-4} Torr, as well as a CCM501 cold cathode ion gauge, which allows for monitoring of the chamber pressure down to 1×10^{-9} Torr. An Apex AX-MC-50SCCM-D mass flow controller regulates the flow of gas admitted into the

chamber. A Bertan 815 -30N high voltage power supply applies the potential difference between the cathode and the grid. A liquid nitrogen cold trap attached to Varian model 0159 diffusion pump is attached to the bottom of the chamber. Attached to the diffusion pump is an Alcatel ZM2008A rotary forepump. The forepump evacuates the chamber to about 1×10^{-3} Torr after which the diffusion pump can evacuate the chamber down to about 1×10^{-7} Torr. The chamber setup can be seen in Figure 10 and Figure 11 and the pump set up can be seen in Figure 12 and Figure 13.
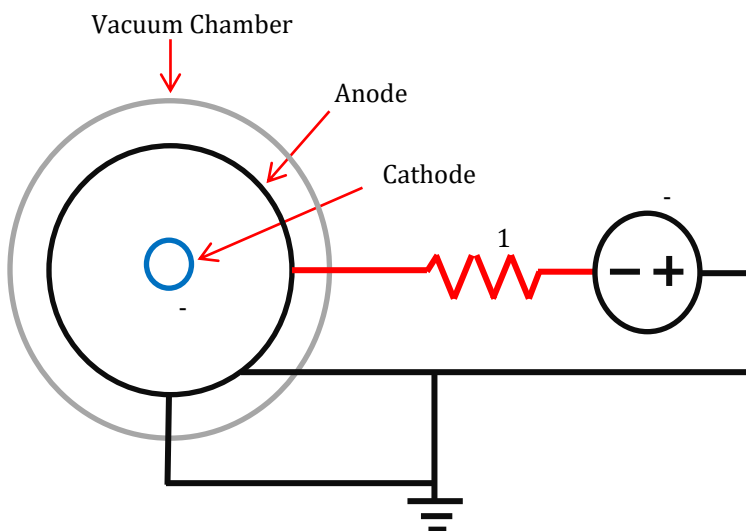

Figure 10. The circuit diagram for the Farnsworth fusor. Shown are the grounded anode grid, the vacuum chamber wall, the cathode grid, the Bertan power supply, and the ballast resistor. Figure from reference [20]
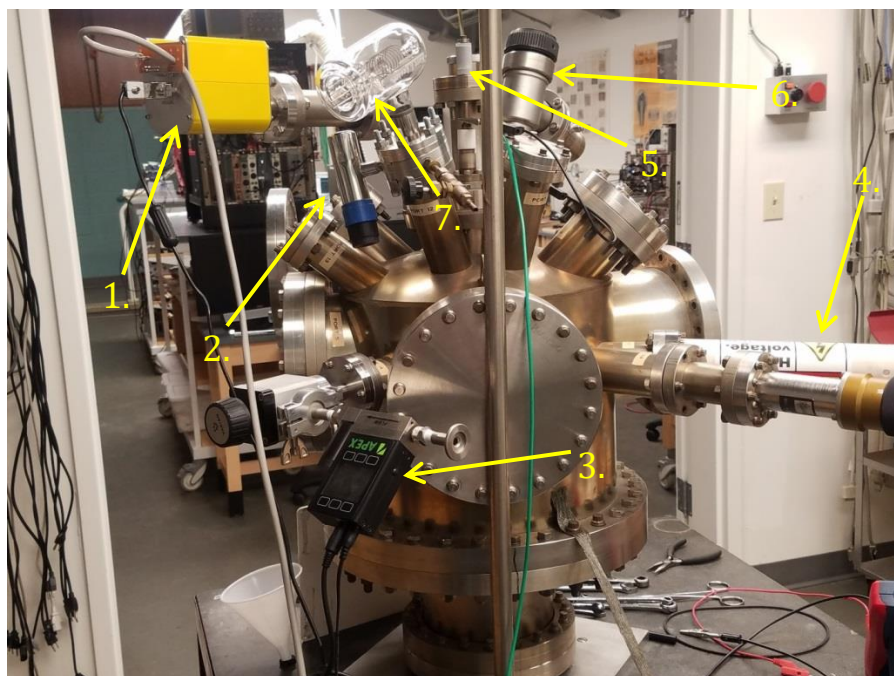
Figure 11. The Houghton College Farnsworth-Hirsch fusor, showing the CCM501 cold cathode ion gauge (1), the pirani gauge (2), the AX-MC-50SCCM-D mass flow controller (3), the high voltage feedthrough (4), the anode linear motion feedthrough (5), the cathode linear motion feedthrough (6) and the hot-cathode ion gauge (7).

Figure 12. The vacuum pump system. (Left) The foreline shut off valve (1) and the foreline up to air valve (2). (Middle) The liquid nitrogen cold trap (3) and the diffusion pump and cooling blower (4). (Right) The Forepump (5).

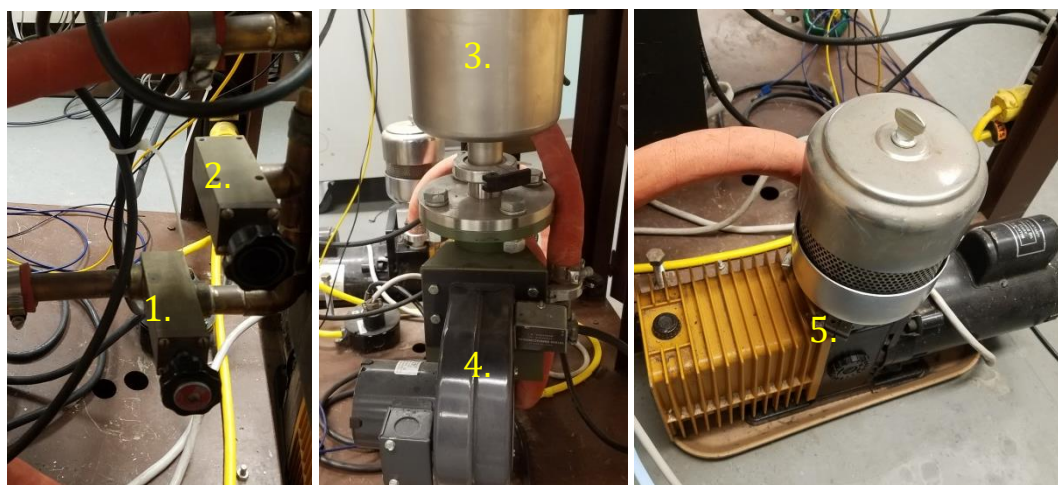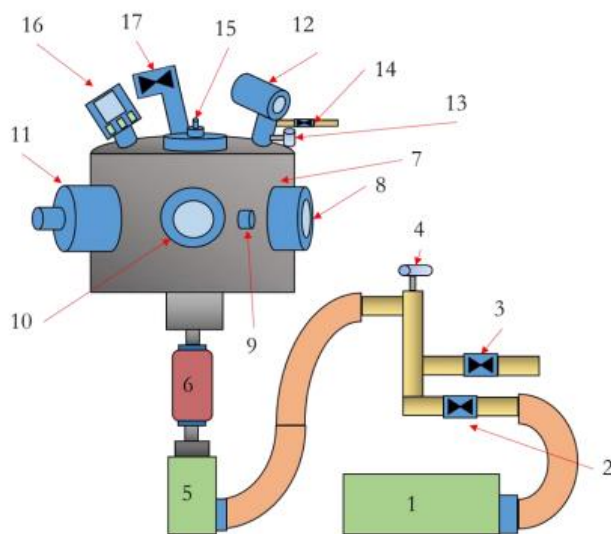Figure 13. The vacuum chamber setup. The forepump (1) evacuates the chamber down to 10^{-3} Torr. The foreline valve (2) disconnects the chamber from the forepump. The up to air valve allows air to enter into the vacuum system (3). A pirani gauge (4) measures the pressure in the foreline. The diffusion pump (5) and the cold trap (6) allow the chamber to be evacuated down to 10^{-7} Torr. The vacuum chamber (7) has various viewports such as viewports (8) and (10), a 2.75 inch conflat port (9), an 8 inch conflat port adapted to a 2.75 inch conflat port (11). A hot cathode ion gauge (12), a cold cathode ion gauge (16) and a pirani gauge (13) are used to measure the chamber pressure. An up to air valve (14) is used to allow air into the chamber. A mass flow controller (17) Figure taken from [21].

Inside the chamber are the grid and the anode, composed of 0.63 mm diameter 304 stainless steel wire. The cathode is a 7.0 cm diameter grid and consists of three 7.0 cm diameter rings that have been welded together. Each ring is arranged such that the three rings form a spherical grid. The cathode is nested within the anode grid, which is consists of 20.3 cm rings and two 15.2 cm rings which have also been welded together to form a spherical grid. Both the anode and the grid can be repositioned by a linear motion feedthrough; additionally the anode is also attached to an electrical feedthrough where the

negative high voltage can be attached and the grid is also connected to the grounded chamber wall. The anode and cathode are nested as shown in Figure 14.

3.2.   The High Voltage System

The high voltage enters the chamber through through a port and is attached to the cathode. To prevent sparking from the high voltage wire to the walls of the chamber, the wire is insulated by ceramic beads which encase the wire as shown in Figure 14.
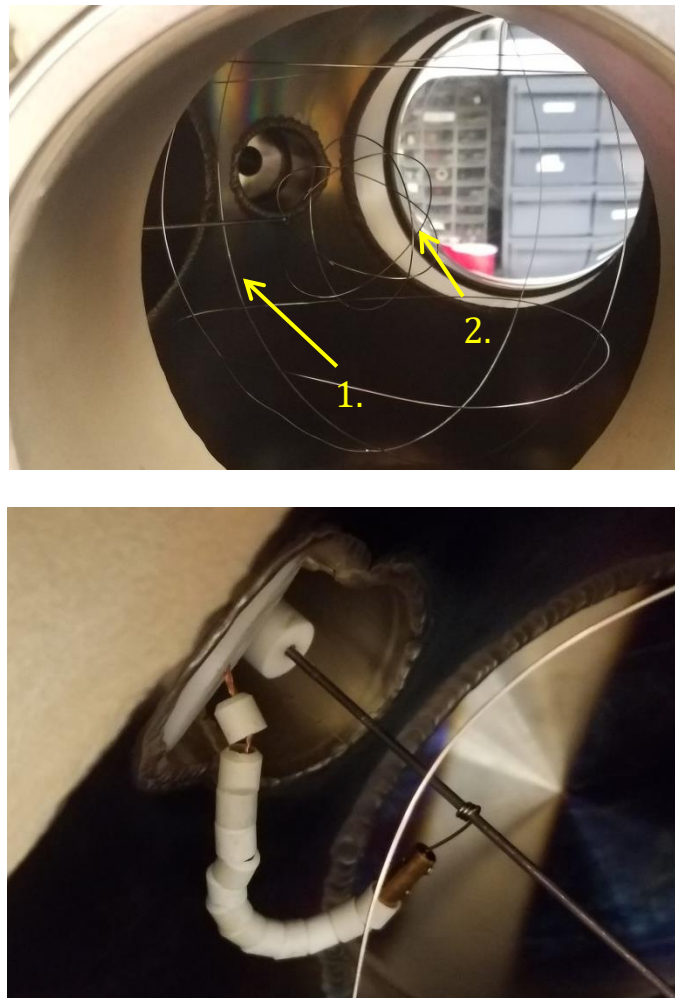

Figure 14. Inside the chamber. (Top) The anode grid (1) and the cathode grid (2). (Bottom) The high voltage feedthrough attached to the cathode grid.

The high voltage is supplied by a Bertan Series 815 -30N, which applies a voltage difference between the cathode and ground as large as -30 kV, and can supply a maximum current of 3.3 mA. The high voltage power supply connects to the inner wire cathode grid through a 1.5 MΩ 7-watt ballast resistor as shown in Figure 10. The ballast resistor serves to lower the potential across the electrodes in order to lower the current during high current flows as would be present during sparking. The high voltage power supply is controlled by applying voltages across pins 1 and 2 and across pins14, and 15 of a DB25 connector on the front panel of the 815 -30N. Pins 1 and 2 control the voltage output of the high voltage power supply, and pins 14 and 15 control the current limit, as described in Table 1. The Hantek PPS2320A power supply has two independent internal power supplies. One power supply in the PPS2320A controls the voltage output of the 815 -30N by applying a 0-5 V difference across pins 1 and 2, corresponding to a 0 to -30 kV on the 815 -30N. The second power supply in the PPS2320A controls the current limit from the 815 -30N by applying a 0-5 V difference across pins 14 and 15 of the 815 -30N, which corresponds to a current limit of 0-3.3 mA. The PPS2320A can be manually controlled using the front panel, but it can also be controlled by a computer via a UE204 USB Portserver connected to a local Ethernet network. In order to be controlled by the computer, the serial interface must be adjusted to the correct baud rate, data bits, stop bits, parity, and termination character, as shown in Table 2.

Once the serial interface has been adjusted to the correct settings, the Hantek power supply can be controlled using commands listed in Table 3.

Table 1. Bertan high voltage power supply pinout. The plus signs correspond to positive voltage and the minus signs correspond to ground.

Pin	Function	Signal	Connection
1	V_{OUT} Program Input (+)	0 to +5 V	Hantek PPS2320A
2	V_{OUT} Program Input (-)	GND	
4	V_{OUT} Program Monitor	0 to +5 V	Mastech M9803R
5	Common (V_{MON} Return)	GND	
10	Logic Common		Connected together to enable HV
11	Enable Input		
14	I_{OUT} Program Input (+)	0 to +5 V	Hantek PPS2320A
15	I_{OUT} Program Input (-)	GND	
17	I_{OUT} Program Monitor	0 to +5 V	Mastech M9803R
18	Common (V_{MON} Return)	GND	

Table 2. Settings for the serial interface for the PPS2320A Hantek power supply and the M9803R Mastech Multimeters.

	Hantek Power Supply	Mastech Multimeters
Baud Rate	9600	9600
Data Bits	8	7
Stop Bits	1	2
Parity	None	None
Term Char	Line Feed (\n)	Line Feed

Table 3. A list of commands for the PPS2320A power supply and the resulting effect. For example, if the command su1200 is sent, then channel 1 on the PPS2320A will be set to 12V.

Command	Effect
suXXXX	Set voltage output for channel 1
siXXXX	Set current limit for channel 1
saXXXX	Set voltage output for channel 2
sdXXXX	Set current limit for channel 2
rv	Read measured voltage of CH1
ra	Read measured current of CH1
ru	Read set voltage of CH1
ri	Read set current limit of CH1
rh	Read measured voltage of CH2
rj	Read measured current of CH2
rk	Read set voltage of CH2
rq	Read set current limit of CH2

The output voltage and current limit for the 815 -30N are proportional to the voltages on pins 1 and 2 and 13 and 14, respectively, from the PPS2320A power supply. The high voltage output of the Bertan 815 -30N can be monitored by two Mastech M9803R multimeters which measure monitor voltages proportional to the high voltage and current, across pins 4 and 5 as well as pins 17 and 18, respectively, as seen in Table 1. The Mastech M9803R communicates with a Digi Portserver TS4 MEI using RS-232 which is in turn connected to a computer through a local Ethernet network. The TS4 MEI Portserver can be read remotely from the computer after enabling RS-232 mode on the front panel. The M9803R requires the serial interface to be set to the correct baud rate, data bits, stop bits, parity, and term char, as listed in Table 2.

3.3.   Controlling and Monitoring the IEC Chamber Pressure

The chamber pressure is monitored by two gauges: a pirani gauge, used for measuring pressures down to 1×10^{-3} Torr, and a cold cathode ion gauge, which can measure pressure down to 1×10^{-7} Torr. The cold cathode ion gauge is controlled by the computer through Ethernet via a TS4 MEI digi Portserver. The cold cathode ion gauge is connected to the TS4 MEI by a RS-485 interface connected as shown in Table 4.

Table 4. Pin configuration to connect the CCM501 Cold Cathode Ion Gauge to the TS4 MEI Digi Portserver via RS-485.

CCM501 Pin	Function	Portserver Pins	Function
1	RS-485 DATA B(+) Input/Output	1	TxD-
		2	RxD-
2	Ground	4	Ground
3	RS-485 DATA A(-) Input/Output	5	TxD+
		6	RxD+

The CCM501 cold cathode ion gauge can be controlled via the front panel. However, by controlling the CCM501 with a computer, it can be used in conjunction with the Apex AX-MC-50SCCM-D mass flow controller to remotely adjust the chamber pressure. The CCM501 must be set to the proper baud rate, data bits, stop bits, parity or term char in order to communicate with a computer as shown in Table 5.

Table 5. The CCM501 cold cathode ion gauge must be set to the settings in the table in order to communicate with the computer

Baud Rate	19200
Data Bits	8
Stop Bits	1
Parity	None
Term Char	Carriage Return (<CR>)

Once the serial interface has been set to the settings for the ion gauge, then the ion gauge high voltage can be remotely enabled or disabled via a command from the computer. Additionally, the status of the ion gauge high voltage can be read back to the computer. Once the high voltage has been enabled, the pressure can be read remotely. The list of commands for the CCM501 cold cathode ion gauge is shown in Table 6.

Table 6. Commands for remotely monitoring chamber pressure with the cold cathode ion gauge.

Command	Description	Command	Response
Read Pressure	Reads current pressure	#01RD	*01_x.xxE-y
Enable High Voltage	Turns on high voltage	#01IG1	*01_PROGM_OK
Disable High Voltage	Turns off high voltage	#01IG0	*01_PROGM_OK
Read Status	Reads if HV is on or off	#01IGS	*01_1_IG_ON, *01_0_IG_Off
Reset	Resets device as if cycling power	#01RST	No response

The chamber pressure is controlled by the AX-MC-50SCCM-D mass flow controller. The mass flow controller can be controlled either using the front panel or it can be controlled

remotely by a computer. The serial interface must be properly configured to allow communication with the mass flow controller, as shown in Table 7.

Table 7. Above are the settings to allow the AX-MC-50SCCM-D mass flow controller to communicate with a computer.

Baud Rate	19200
Data Bits	8
Stop Bits	1
Parity	None
Term Char	Carriage Return (<CR>)

Once the serial interface has been set to communicate with the mass flow controller, the set point can be remotely set from the computer. Changing the set point changes the rate the mass flow controller lets gas into the chamber. For a desired flow rate, the set point can be determined by:

$$Value = \frac{Desired\ Set\ Point\ (slpm) \times 64000}{65535} \qquad (3.3.1)$$

where slpm is standard liters per minute. As an example, for a desired flow rate of 3600 slpm, the set point is (3600 × 64000 / 65535) = 3516 where 65535 is the full scale flow range, and the proper command to set the flow rate to 3600 slpm would be A3516 as shown in Table 8.

Once the set point is set, the mass flow controller's default setting is polling mode, where the device measures data, but does not send that data to the computer unless polled directly. The command *@=@ can be used to switch to streaming mode, where a

continuous stream of data is sent to the computer; the command *@=A can be used to switch the device back to polling mode. Entering the command A polls the device:

Table 8. The table above lists the commands for controlling the mass flow controller.

Switch to Streaming Mode	*@=@
Switch to Polling Mode	*@=A
Poll the Device	A
Set the Set Point Value	A#####

3.4. LabView Control Interface

As discussed in the previous sections, the fusor is set up to be remotely operated from a computer using LabView. The control program creates a front panel, allowing researchers to adjust values such as pressure or high voltage.

Unfortunately, the "instrument assistants" in the code controlling the cold cathode ion gauge, which allow the code to communicate with the device, generate an error message when the computer attempts to communicate with the ion gauge. It is unclear whether this is due to an actual error in the code itself, is outdated because of changes in how LabView operates, is due to a change between how Windows XP and Windows 10, or is because of an inadvertent hardware change. The code had worked previously on Windows XP, however, the problem of the code sending a hex error also arose while using Windows 7.
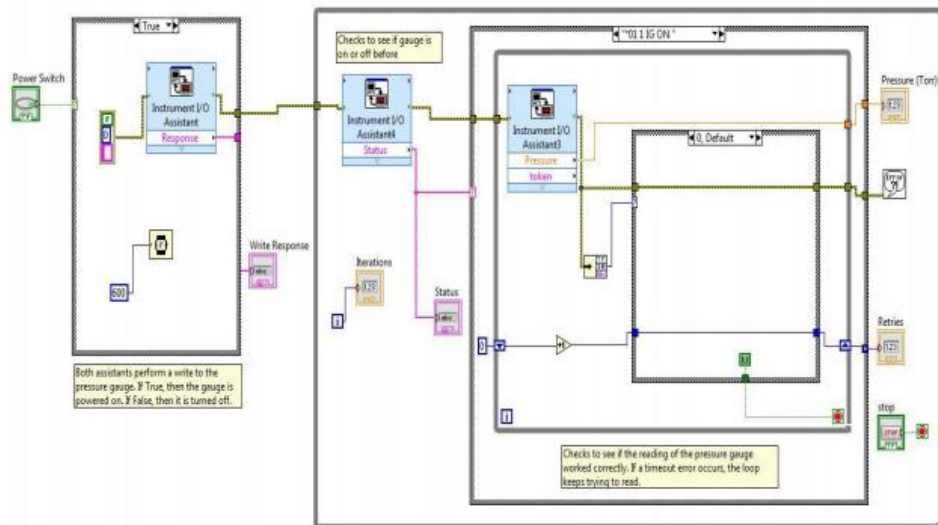
Figure 15. The code controlling the cold cathode ion gauge. The code is designed to turn on the high voltage for the ion gauge, then continually read the pressure via a for loop [22].

While still using Windows XP, the code was designed such that the VI in Figure 15 would send a signal to the cold cathode ion gauge to check whether or not it the high voltage for the device was on. If the high voltage was not on, another signal would be sent to turn on the high voltage, and then the pressure from the device would constantly be read out to the computer. Similarly, there was a VI for controlling the mass flow controller which would send a signal to an "Instrument Assistant" to set the set-point, or would send a signal to another "Instrument Assistant" to read from the device. There was also a VI for controlling the power supply. A signal would be sent to "Instrument Assistants" to read out the values of the voltage and current monitor, and a signal would also be sent to the power supply to change the voltage across pins 1 and 2 and pins 14 and 15. Researchers had hoped to combine the VIs into one VI, however before this could happen, Houghton College changed to Windows 7.

Chapter 4

CURRENT RESEARCH

In this section, the results from testing the high voltage power supply will be presented, as well as the calibration of the pressure gauges.

4.1.   High Voltage Calibration

The fusor is designed to be remotely operated. However, LabView is currently unable to properly communicate with some components of the fusor, either due to compatibility issues with the newer versions of LabView or because of compatibility issues with Windows 10. The fusor can be operated manually however, and so components other than the code were tested. All devices for controlling the fusor were tested via a front panel except the pumps, which were monitored using the ion gauge, and the Bertan 815 -30N high voltage power supply. Prior to use, the high voltage power supply and the mass flow controller were calibrated. The mass flow controller allows gas into the chamber at a controlled rate. A given input for the mass flow controller, and therefore a given rate of gas entering the chamber, resulted in a corresponding chamber pressure. To calibrate this, the chamber pressure was measured as a function of the mass flow controller settings. Similarly, the high voltage power supply required calibration: the voltage output and current limit is set by the voltage output from the Hantek power supply. To calibrate this, the high voltage was measured as a function of the set voltage on the Bertan power supply.

4.1.1. Construction of the Voltage Divider

To measure the voltage and current output of the high voltage power supply, a voltage divider circuit was created. A standard voltmeter is not capable of measuring 30 kV,

however, by using a voltage divider, it is possible to measure a smaller potential drop across a resistor and calculate the high voltage and current.

Because the Bertan high voltage power supply is capable of supplying up to -30 kV, it was crucial that the voltage divider be insulated against sparking. Initially a grounded metal can surrounding the resistor chain was used. The metal walls of the can were grounded to allow researchers to measure the potential and current safely, and the radius of the can insulated the wire from sparking due to the ample amounts of air filled space between the resistor chain and the walls of the can. Unfortunately, the large resistances used in the resistor chain did not draw enough current to test the power supply at milliamp currents. In order to draw 3.3 mA at 30 kV, the resistor chain needed to have lower resistances and therefore dissipate more power, requiring longer resistors, so the grounded metal can was no longer large enough. Instead, an approximately 2.2 ft. long, 3 in. diameter PVC pipe (Figure 17) was used. The pipe and the air provided enough insulation to prevent sparking. The voltage divider was designed using twenty 512 kΩ, 5 W resistors and one 2 kΩ resistor connected in series. The diagram of the new voltage divider circuit is shown in Figure 16. The maximum potential across each 512 kΩ resistor was 1.5 kV, which is small enough to prevent sparking between resistors.
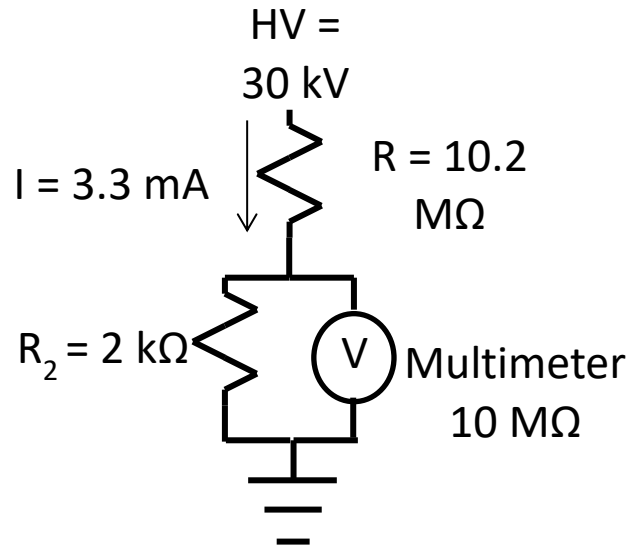
Figure 16. The circuit diagram for the voltage divider. The maximum high voltage was 30 kV and a current was 3.3 mA. The 10.2 MΩ resistor consists of 20 512 kΩ resistors in series. The internal resistance of the multimeter is 10 MΩ.

Figure 17. The voltage divider. The negative high voltage attaches to the top through a banana Jack, and potential is measured across a 2 kΩ resistor via a banana adapter at the bottom. The divider is grounded at via a banana jack at the bottom.

The voltage divider is designed to dissipate the power across each resistor. The total power dissipated by the voltage divider when the power supply is operating at 30 kV is 100 W. The total power dissipated by each 512 kΩ resistor is 4.93 W, so resistors were selected that could dissipate 5 W. Because the power dissipated by the 2 kΩ resistor and the multimeter was so small, a small resistor could be used. Using Ohm's Law and the values of each resistor, the value of the high voltage was determined to be 5122 times the value of the voltage measured by the multimeter.

4.1.2. Voltage and Current Calibration

In order to calibrate the high voltage, the voltage monitor on pin 4 of the Bertan power supply was compared to the measured high voltage output as shown in Figure 18.
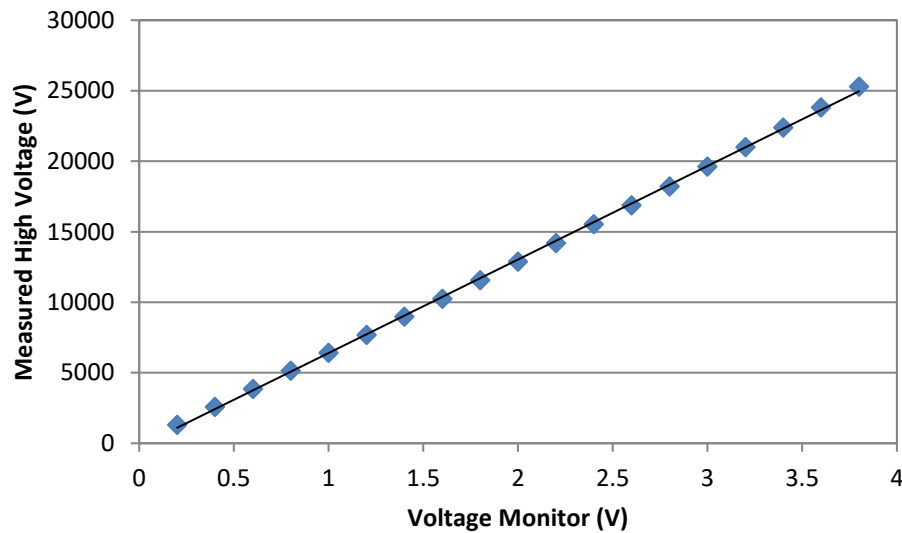

Figure 18. The voltage calibration curve. The measured output voltage is plotted as a function of the voltage monitor input to pin 4 the best fit linear calibration is y = 6629.7x – 229.05.

The current should be calibrated by plotting the measured output current as a function of the current monitor on pin 16, as shown in Figure 19.
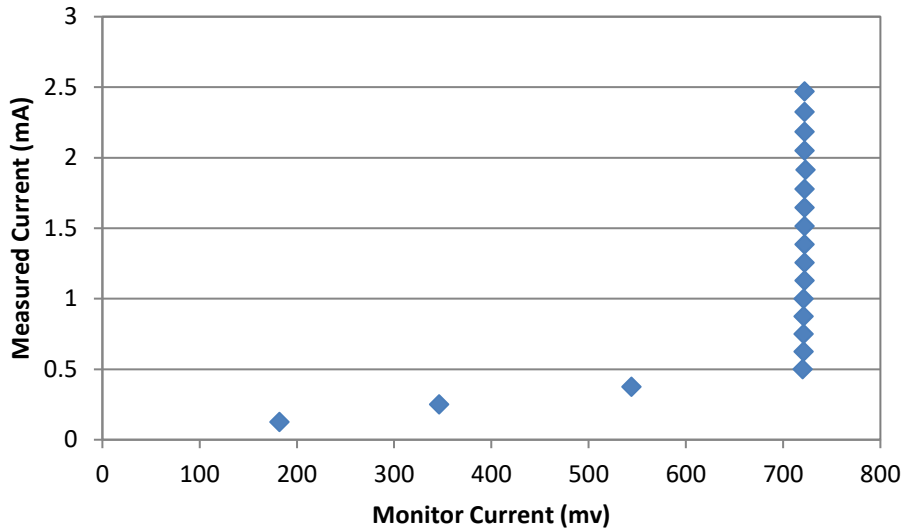

Figure 19. The measured current as a function of monitor current from pin 16, which is the output voltage sent from the Bertan series power supply that is proportional to the current output from the high voltage power supply.

The measured current correlated linearly with the monitor current until approximately 0.5 mA at which point the current continued to increase but the monitor current remained constant. The plot demonstrates that the current monitor function of the Bertan power supply is not working properly. Because of this, the current must be measured directly with an ammeter. This is difficult because the ammeter will have to be floated at 30 kV.

4.1.3. Pressure gauge calibration

The chamber pressure can be controlled by changing the set point of the mass flow controller, and measured using the cold cathode ion gauge. In order to know how to set the

set point, the chamber was pumped down to 1×10^{-5} Torr, the set point was varied and

the pressure was measured using the both cold cathode ion gauge and the hot cathode ion

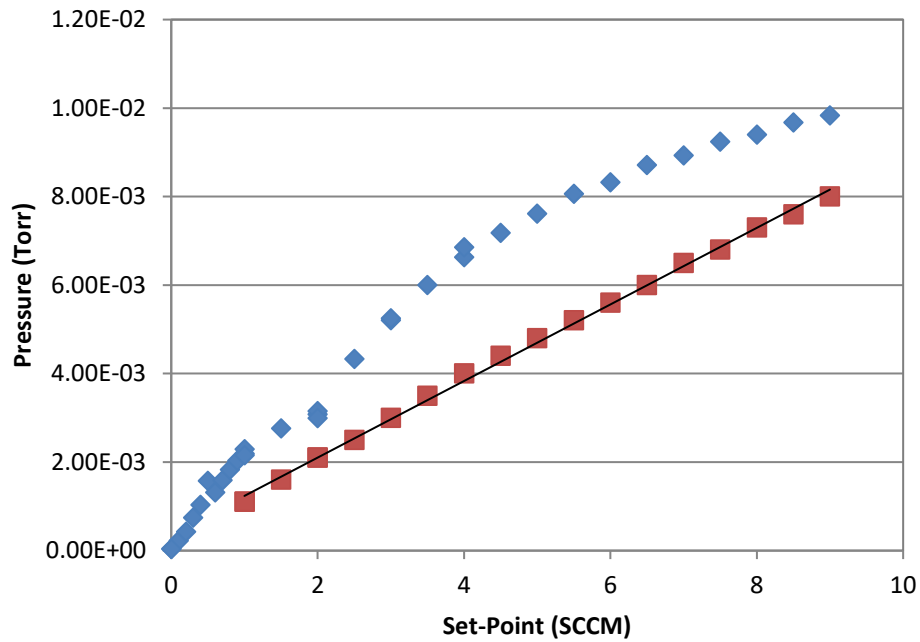gauge. The results are shown in Figure 20.

Figure 20. Chamber Pressure as a function of Set-Point. The pressure measured by the Cold Cathode Ion Gauge (blue diamonds) and the Hot Cathode Ion gauge (red squares) as a function of the Set-Point. The cold cathode ion gauge is not linearly correlated to the set point for the mass flow controller. A linear fit of the hot-cathode ion gauge as a function of the MFC Set-Point gives y = 0.00009x + 0.00040.

The cold cathode ion gauge pressure was measured again over the lower pressure range
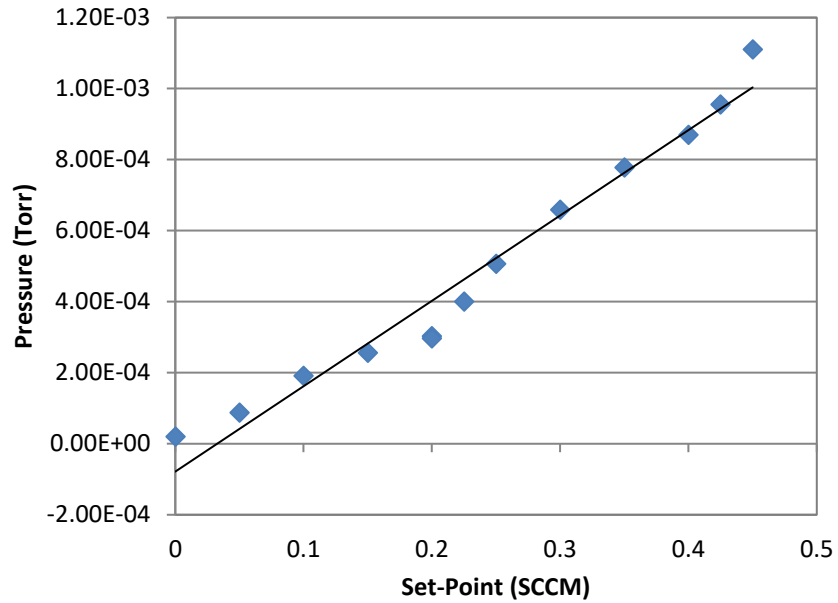
shown in Figure 21, and was found to be roughly linear.

Figure 21. Cold Cathode Ion Gauge pressure as a function of the Set-Point. The equation relating the pressure and the Set-Point is y = 0.00240x − 0.00008.

4.2.   Sparking Prevention

Sparking was found to be an issue at the port where the high voltage electrical feedthrough connected to the inner grid. This was because the electrical feedthrough is close to the walls of the port. In an attempt to prevent this, the high voltage wire had been insulated with ceramic beads, however, the beads were insufficient to prevent sparking. As a further attempt, two nylon disks were machined in order to keep the high voltage wire away from the walls of the chamber port, as shown in Figure 14 and Figure 22. Testing the chamber with high voltage is necessary to test whether the nylon disks can prevent sparking.
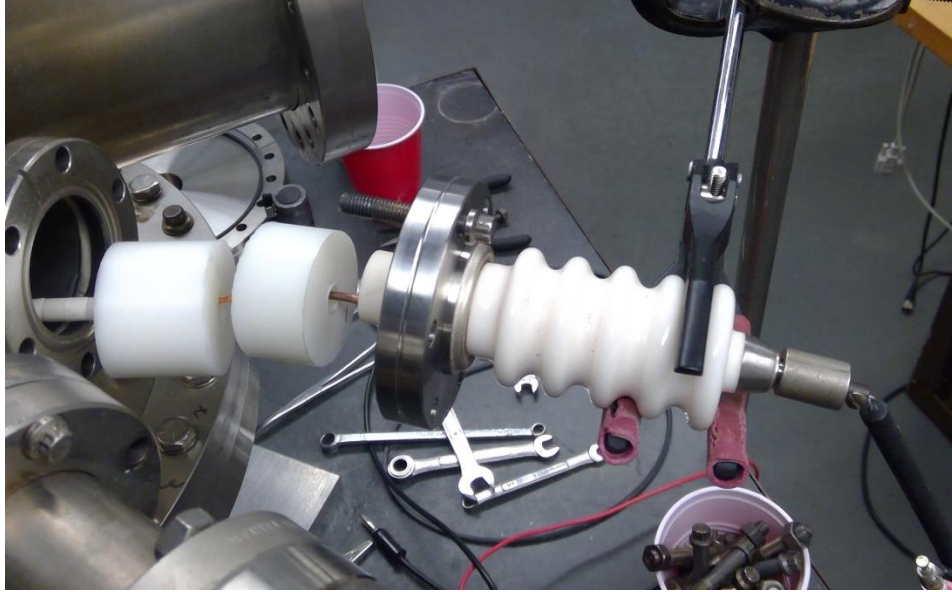
Figure 22. High voltage electrical feedthrough insulation. Nylon disks are used to keep the wire equidistant from the chamber port wall.

Chapter 5

RESULTS AND FUTURE RESEARCH

As recently as 2016 the fusor was working while using air. However, Houghton College
required computers to be upgraded from Windows XP to Windows 7. This change required
researchers to upgrade to LabView 2014, which could not read the files created using older
versions of LabView. Because of this, the LabView code controlling the fusor had to be
rewritten. Since updating to Windows 7, the fusor has not worked. Much progress has been
made towards fixing the Houghton College IEC fusor, however there is still much work to
be done before the fusor is operational. In this section, the current status of the IEC fusor
will be evaluated and the plans for future research will be discussed.

5.1.   Current Status

Currently, the Houghton College Farnsworth Fusor is not operational, although many
components can be operated manually. The Hantek power supply can be controlled by the
front panel, which provides the programming voltage to the Bertan high voltage power
supply, and can be controlled remotely using the user interface HyperTerminal or NI MAX.
When trying to control it using LabView the Instrument Assistant generates an error
message and the LabView VI (virtual instrument) crashes, and must be stopped and run
again to continue using the code to control the power supply.

The Mastech multimeters, which read the monitor voltage and monitor current outputs of
the Bertan high voltage power supply, are operational both using the front panel and by

communication via the computer with LabView. The LabView code simply reads values from the multimeters.

The cold cathode ion gauge currently reads pressure via the front panel, however, it will not communicate with an Instrument Assistant in LabView. Although originally able to communicate with the computer via NI MAX and HyperTerminal, the ion gauge does not currently communicate with the computer through any interface, which is most likely due to the RS-485 connection between the ion gauge and the digi Portserver.

The Apex mass flow controller can control the gas allowed into the chamber using the front panel, NI MAX, HyperTerminal, and LabView. The LabView code is designed to set the mass flow controller to polling mode and to send commands to the device to change the set point.

The Bertan power supply does not have a front panel, but can be controlled by changing the input voltages sent from the Hantek power supply. Currently, the Bertan power supply cannot be controlled from the computer because the Hantek power supply cannot be controlled by the computer via LabView. Additionally, the current monitor voltage output that is proportional to the current supplied Bertan power supply does not work properly.

5.2. Future Plans

There are many things to still be done with the Farnsworth fusor. First, the code controlling its various components must be fixed. Because of mandatory upgrades required by the

college, the code must now be transferred yet again from the original Windows 7 computer to a computer operating with Windows 10. Because the current monitor on the Bertan high voltage power supply is broken, there must be some method for remotely measuring the current output from the high voltage power supply. Finally, the chamber sparking must be fixed. Once each of these has been accomplished, the fusor experiments will be carried out first with air, then hydrogen, and finally deuterium.

The code is one of the largest obstacles to the remote operation of the Houghton College Farnsworth fusor, which is necessary for radiation protection if x-rays are allowed to exit the chamber. Additionally, Houghton College is interested in being able to produce neutrons with the Farnsworth Fusor, which further increases the need for remote operation. The Instrument Assistants used in LabView are unable to communicate with the devices, and this inability to communicate must be addressed in order to operate the fusor. Additionally, each individual piece of code for controlling individual devices must be combined into one VI to automate operation of the fusor.

The LabView code is not the only problem with controlling the fusor remotely with a computer. The fusor was originally sucessfully operated using a computer with Windows XP installed. However, when Microsoft ended XP support, the college required all computers to upgrade to Windows 7. After a few years, Microsoft ended Windows 7 support, and all control systems must be transferred to Windows 10. Additionally, all of the old LabView 8 code designed to work with Windows XP and modified to work properly with Windows 7 must now be rewritten to work with Windows 10 and Labview 2014.

Another problem that prevents the remote operation of the Houghton College Farnsworth fusor is the inability to accurately measure the Bertan series power supply current output. Because the Bertan power supply current monitor output is no longer proportional to the output current, the only way to measure the current going into the Farnsworth fusor is to float an ammeter at -30 kV, which will be difficult to interface to the computer. The easiest way to fix this would most likely be to replace the Bertan power supply. However, replacing the power supply would be costly and require further modifications to the code.

The desired end result is being able to remotely operate the Farnsworth fusor and to use it to fuse deuterium, like the reaction shown in Figure 1. One of the two possible D-D reactions would produce ^{3}He and a neutron, the cross section for which is shown in Figure 23. As can be seen, the cross-section for this reaction is significant at 30 kV, which is the potential difference between the two electrodes. Because of this, the fusor could be used as a neutron source for other experiments, and would allow research with fusion reactions, as well as a way to test the models for plasma flow and electric potential inside the fusor. Much work is still required before this is possible, and further research is still needed for the operation of the Houghton College Farnsworth fusor.
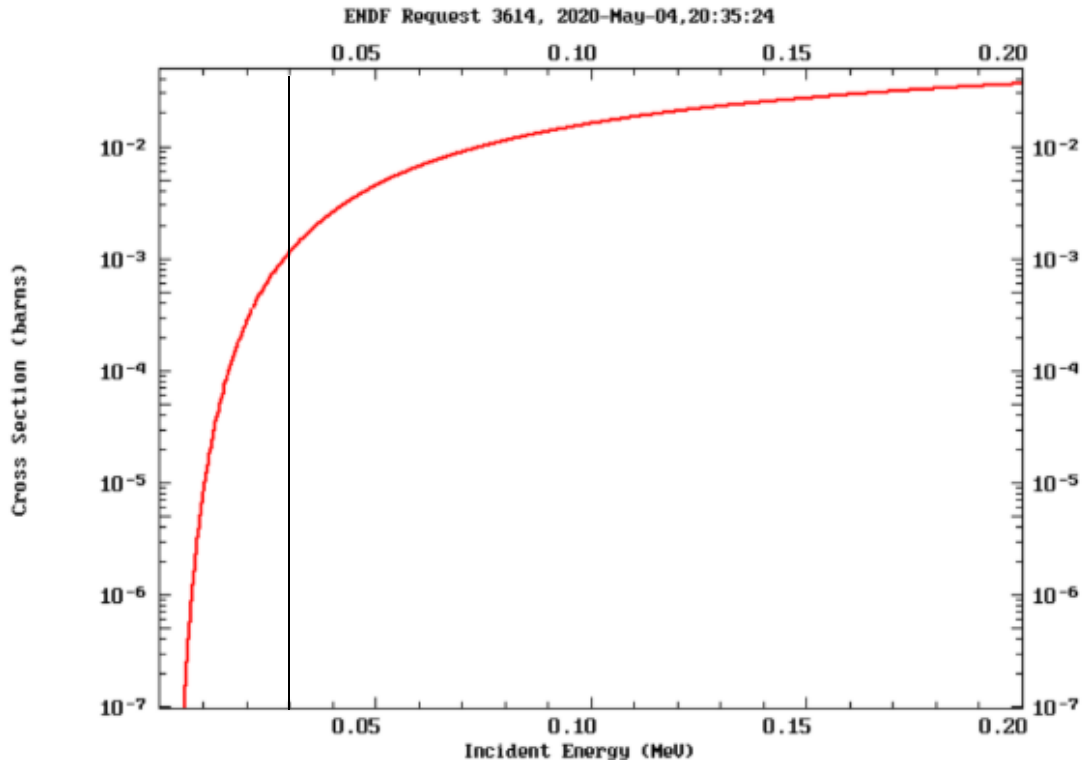
Figure 23. Cross Section ^{2}H(d, n)^{3}He as a function of incident energy. The vertical black line represents 30 kV, which is the potential difference supplied by the Bertan power supply, and therefore the potential difference across which electrons and ions are accelerated. Figure from Reference [23]

References

[1] V. D. Shafranov, On the History of Research into Controlled Thermonuclear Fusion. Phys-Uspekhi, 44 (8) 835-865 (2001) https://fire.pppl.gov/rf_shafranov.pdf

[2] K. Zuvela, I. Adlington, S. S. Aljunied, J. Edwards, Determining the best approach to commercial fusion power. (2014) https://epress.lib.uts.edu.au/student-journals/index.php/PAMR/article/view/1383/1464

[3] EUROfusion. https://www.euro-fusion.org/devices/jet/

[4] ITER. https://www.iter.org/mach

[5] L. Spitze, A Proposed Stellarator. U S Atomic Energy Commission (1951) https://diglib.princeton.edu/pdfs/PPL001/c0002.pdf

[6] R. C. Wolf, et al, Performance of Wendelstein 7-X Stellarator Plasmas During the first Diverter Operation Phase. Physics of Plasmas 26, 082504. (2019) https://aip.scitation.org/doi/10.1063/1.5098761

[7] University of Rochester, World's Most Powerful Ultraviolet Laser Comes On-line. (1995) http://www.rochester.edu/pr/releases/lle/omegadun.htm

[8] J. Lindl, B. Hammel, Recent Advances in Indirect Drive ICF Target Physics. (2004) https://fire.pppl.gov/iaea04_lindl.pdf

[9] National Ignition Facility, NIF sets new laser Energy Record. (2018) https://www.llnl.gov/news/nif-sets-new-laser-energy-record#:~:text=The%20NIF%20laser%20uses%20tens,the%2010-meter%20tar

[10] P. T. Farnsworth, Electric discharge device for producing interactions between nuclei. US Patent 3,258,402 (1966)

[11] S. Earnshaw, On the Nature of the Molecular Forces which regulate the Constitution of the Luminiferous Ether. (1839) https://www.mit.edu/~kardar/research/seminars/Casimir2010/pdf/EarnshawPaper.pdf

[12]University of Wisconsin-Madison, Inertial Electrostatic Confinement Fusion. (2014) https://iec.neep.wisc.edu/publications.php

[13]R. Sedwick, Project: Multi-grid Inertial Electrostatic Confinement Fusion (IECF). (2020) http://sppl.umd.edu/projects/multigrid/

[14] P. T. Farnsworth, Method and apparatus for producing nuclear-fusion reactions. US Patent 3386883A (1968)

[15] R. L. Hirsch, G. A. Meeks, Apparatus for generating fusion reactions. US Patent 3530497 (1970)

[16] J. D. Callen, *Fundamentals of Plasma Physics,* (University of Wisconsin-Madison), WWW Document http://homepages.cae.wisc.edu/~callen/chap5.pdf, 2003. (Unpublished), pg. 2.

[17] J. D. Callen, *Fundamentals of Plasma Physics,* (University of Wisconsin-Madison), WWW Document http://homepages.cae.wisc.edu/~callen/chap5.pdf, 2003. (Unpublished), pg. 6.

[18] J. D. Callen, *Fundamentals of Plasma Physics,* (University of Wisconsin-Madison), WWW Document http://homepages.cae.wisc.edu/~callen/chap5.pdf, 2003. (Unpublished), pg. 11.

[19] J. D. Callen, *Fundamentals of Plasma Physics,* (University of Wisconsin-Madison), WWW Document http://homepages.cae.wisc.edu/~callen/chap5.pdf, 2003. (Unpublished), pg. 11.

[20] I. Love, Undergraduate Thesis, Houghton College, 2014, Pg. 35.

[21] I. Love, Undergraduate Thesis, Houghton College, 2014, Pg. 29.

[22] K. Craft, Undergraduate Thesis, Houghton College, 2016, pg. 41.
[23] D. A. Brown et. al. Nucl. Data Sheets 148(2018)1